

# Theory of magnetism for rare-earth magnets on the Shastry-Sutherland lattice with non-Kramers ions

Guijing Duan,<sup>1</sup> Rong Yu,<sup>1,2,\*</sup> and Changle Liu<sup>3,†</sup>

<sup>1</sup>*School of Physics and Beijing Key Laboratory of Opto-electronic Functional Materials & Micro-nano Devices, Renmin University of China, Beijing 100872, China*

<sup>2</sup>*Key Laboratory of Quantum State Construction and Manipulation (Ministry of Education), Renmin University of China, Beijing, 100872, China*

<sup>3</sup>*School of Engineering, Dali University, Dali, Yunnan 671003, China*

(Dated: December 6, 2024)

Motivated by the rapid experimental progress on the rare-earth Shastry-Sutherland lattice magnets, we propose a generic effective spin model that describes interacting non-Kramers local moments on the Shastry-Sutherland lattice. We point out that the local moments consist of both magnetic dipole and quadrupole components and the effective model turns out to be an extended XYZ model with an intrinsic field that accounts for the crystal field splitting. We then study the ground-state phase diagram of the model and find that pure quadrupole orders, which are invisible to conventional experimental probes, can be stabilized over a broad regime. In particular, we show that a hidden “1/3 magnetization plateau” with quadrupole orders generally exists and discuss its experimental signatures. Finally, we discuss the relevance of our results to the rare-earth Shastry-Sutherland lattice magnets  $\text{Pr}_2\text{Ga}_2\text{BeO}_7$  and  $\text{Pr}_2\text{Be}_2\text{GeO}_7$ .

## I. INTRODUCTION

Geometrically frustrated quantum magnets emerge as a playground to study various unconventional quantum phenomena characterized by suppressed long-range magnetic order and peculiar low-energy dynamical behaviors [1–3]. One prominent example is the Shastry-Sutherland lattice (SSL) magnets, which host a variety of novel phases owing to the strongly frustrated interactions between localized magnetic moments. This system consists of orthogonal spin dimers with frustrated inter-dimer interactions on a two-dimensional (2D) lattice [4]. Experimentally, it has been widely recognized that the low-temperature phases of the quantum magnet  $\text{SrCu}_2(\text{BO}_3)_2$  can be well described by the  $S = 1/2$  AFM Heisenberg model on the SSL. In this compound, the competing interactions result in a dimer singlets (DS) ground state where spin dimers along the diagonal bonds form singlets [5]. By applying a hydrostatic pressure, the system undergoes a phase transition to a plaquette valence bond solid (PVBS) and then to a Néel antiferromagnetic (AFM) ordered state [6, 7]. The presence of PBVS-to-AFM phase transition makes this system an ideal experimental platform to investigate the exotic physics of deconfined quantum criticality (DQC) [8–10]. Moreover, the ground state can also be tuned by applying an external magnetic field, where various fractional magnetization plateaus emerge, reflecting the strong geometrical frustration in this system [11–13].

Recently, research interest on quantum magnetism has been extended to systems with strong spin-orbit coupling (SOC) [14–25]. In these systems, the effective moments are formed by a combination of spin and orbital angular momenta, and the interactions among the moments are usually anisotropic in both real space and spin space. This exchange anisotropy

can induce dynamic frustration, resulting highly non-trivial quantum phases of matter such as quantum spin liquids (QSL) [2, 3, 14, 15], where local moments remain highly correlated while strongly fluctuating. Following such spirit, there have been quite intense experimental and theoretical activities on exploration of relevant systems, such as honeycomb Kitaev magnets [16–18], pyrochlore spin ice [19, 20], and triangular lattice materials [21]. Moreover, in strong SOC magnets the moments may contain high-order multipolar components, such as quadrupoles and octupoles [22–24]. This can give rise to a rich variety of novel phases and quantum critical behaviors. However, multipolar moments and their ordering cannot be directly probed by traditional experimental techniques, such as neutron diffraction. This puts a crucial challenge on how to detect these hidden phases experimentally [22–25].

To gain a deeper understanding on the experimental behaviors of such strong SOC materials, it is essential to construct microscopic models that are able to properly describe the interacting local moments. Microscopic theories on Kitaev, pyrochlore and triangular lattice materials have been well developed [20, 22, 23]. However, existing theory for magnets on the SSL are still limited to strongly Ising anisotropic systems ( $\text{TmB}_4$ , etc.) [26–34]. A generic model describing the full source of quantum fluctuations in SSL systems is highly demanded given the growing experimental reports on relevant materials recently [35–40].

The major difficulty in constructing a generic theory of strong spin-orbit-coupled SSL magnets comes from the low crystal symmetry of these systems. As a comparison, for the extensively studied triangular/honeycomb/pyrochlore lattice systems, the point group symmetry at the magnetic ion contains at least a three-fold rotation. The rotational symmetry puts strong restrictions on the form of crystal field wave functions, and constrains the magnetic moment directions along or perpendicular to the three-fold axis. Moreover, they also strongly restrict the form of interactions and the number of model parameters, making the effective Hamiltonian of relatively simple and convenient for numerical studies. On the

\* rong.yu@ruc.edu.cn

† liuchangle89@gmail.com

other hand, for Shastry-Sutherland magnets, the symmetry of crystal field environment around rare-earth ions is much lower. For example,  $\text{RE}_2\text{Ga}_2\text{BeO}_7$  and  $\text{RE}_2\text{Be}_2\text{XO}_7$  ( $X=\text{Si}, \text{Ge}$ ) [35, 37, 39, 40] the local environment of  $\text{RE}^{3+}$  only contains no rotational symmetry but only a mirror reflection (as marked in Fig. 1). As a consequence of the low symmetry, the directions of the local moments are no longer fixed to be parallel or perpendicular to the crystal plane, but in general form a certain angle with respect to the crystal plane, where the angle is determined by the detail of crystal field wave functions. Moreover, the multi-sublattice structure of the SSL makes the angle sublattice dependent, which further complicates the analysis of experimental data and the modeling.

In this paper, we develop a generic effective spin model for rare-earth Shastry-Sutherland magnets. For clarity, in this work we only consider the case of non-Kramers magnetic ions, and the Kramers case will be discussed in a separate work [41]. For Kramers ions, the crystal field levels always form degenerate Kramers doublets protected by the time-reversal symmetry. However, for non-Kramers ions there is no symmetry to protect any crystal field degeneracy, namely, all crystal field levels are in principal non-degenerate singlets. The presence of crystal field splitting generates an intrinsic field for the local moments. In addition, for a non-Kramers moment only one component (denoted as longitudinal) behaves as a magnetic dipole, while the other two components (transverse ones) are even under the time reversal symmetry and behave as quadrupoles. Based on symmetry analysis, we find that the effective spin model takes the form of an extended XYZ model supplemented by an intrinsic field that originating from the crystal field splitting. To reveal the physical roles of the XYZ exchange anisotropy and the intrinsic field respectively, we first switch off the intrinsic field in the model and discuss the phase diagram in the presence of XXZ- and XYZ-type anisotropy. Then we examine the influence of the intrinsic field to the XYZ anisotropic model. Given that the effective spin model has too many model parameters, obtaining a full phase diagram is impractical. To manage computational complexity, we have selected a few representative parameter points and explore the implications of the intrinsic field, respectively. This approach allows us to gain insights into the underlying physics without the need for exhaustive computational resources.

The rest of the paper is organized as follows. In Sec. II, we provide a symmetry analysis on the structure of local moments and derive the effective Hamiltonian. In Sec. III we explore how the system couples to the magnetic field. As a result of the sublattice dependent local moment environment, this coupling is quite different from ordinary spin systems, leading to a complicated magnetic response to the applied field. We discuss how to extract information about the exchange couplings from magnetic susceptibility measurements. In Sec. IV we present the numerical phase diagram demonstrating the implications of XXZ- and XYZ-type exchange anisotropy as well as the intrinsic field, respectively. Due to the quadrupolar nature of the transverse spin components, several quadrupolar ordered states can be stabilized in the phase diagram. Although the quadrupolar order parameters are not directly ob-

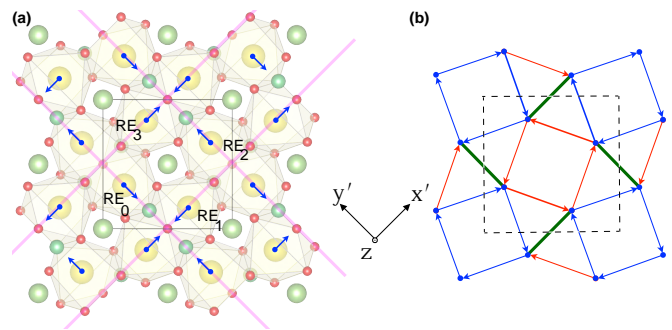


Figure 1. Crystal structure of  $\text{RE}_2\text{Ga}_2\text{BeO}_7$  and sketch of the SSL. (a).  $\text{RE}^{3+}$  and  $\text{O}^{2-}$  are denoted by yellow and red balls, respectively. Mirror planes of  $\text{RE}^{3+}$  are indicated by purple lines. The in-plane direction of the local dipole axes  $\mathbf{n}_i$  are labeled by blue arrows. (b). The intra-dimer bonds of the SSL are indicated by thick dark green lines. The  $\eta_{ij} = \pm 1$  inter-dimer bonds in Eq. (2) are marked as red and blue, respectively, with the directions  $i \rightarrow j$  are marked by arrows.

servable in most conventional probes, the underlying structures of these hidden orders are reflected in the dynamical excitation spectra, which are visible via neutron and light scattering measurements. In Sec. V we summarize our results and discuss the relevance of our work to a number of rare-earth SSL magnets recently reported, including  $\text{Pr}_2\text{Be}_2\text{GeO}_7$  and  $\text{Pr}_2\text{Ga}_2\text{BeO}_7$ .

## II. GENERIC EFFECTIVE SPIN MODEL

### A. Crystal field scheme

For definity, we consider the crystal structure of SSL compounds  $\text{RE}_2\text{Be}_2\text{GeO}_7$ , where  $\text{RE}^{3+}$  refers to non-Kramers ions,  $\text{RE}=\text{Pr}, \text{Sm}, \text{Tb}, \text{Ho}, \text{Tm}$ . Here we take  $\text{RE}=\text{Pr}$  as an example to illustrate the crystal field scheme (shown in Fig. 2). The non-Kramers  $\text{Pr}^{3+}$  ion has total orbital angular momentum  $L = 5$  and total spin angular momentum  $S = 1$ . The strong spin-orbit coupling couples  $L$  and  $S$  to the total angular momentum  $\mathcal{J} = 4$ . In a crystal field environment, these nine-fold multiplets further split into various crystal field levels. Since the point group symmetry of the  $\text{Pr}^{3+}$  site contains only a mirror reflection (mirror planes shown by purple lines in Fig. 2), all crystal field levels form non-degenerate singlets [40]. If the crystal field gap were sufficiently large, the low-energy property of the system would be dominant by the lowest singlet with effective spin zero, and hence we would not expect any magnetism. However, in experiments the system become magnetized under external magnetic field, and in thermodynamic measurements the magnetic entropy saturates to  $\sim 0.89R \ln 2$  at around 15 K [40]. These strongly implies that the magnetism is contributed by a quasi-doublet CEF ground states, which are well separated in energy to other excited crystal field levels, as illustrated in Fig. 2.

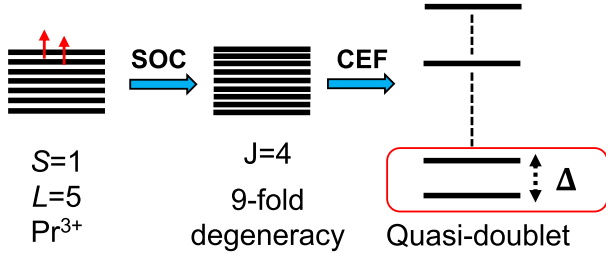


Figure 2. Crystal field scheme of  $\text{Pr}^{3+}$  in the rare-earth SSL magnet  $\text{Pr}_2\text{Be}_2\text{GeO}_7$ . The red arrows refer to Pr 4f electrons. The SOC couples orbital and spin angular momenta  $L$  and  $S$  to the total angular momentum  $J = 4$ . Under crystal electric field (CEF) the 9-fold multiplet corresponding to  $J = 4$  further splits to 9 non-degenerate singlets. The two lowest crystal levels (enclosed by the red box) are close in energy and form a quasi-doublet which is well separated in energy to other crystal field levels. This quasi-doublet accounts for the low-temperature magnetism of the material.

### B. Local moment structures

The local moment structures of non-Kramers ions can be analyzed from symmetries of the crystal field levels. We define the  $z$  direction to be perpendicular to the plane of local moments, and  $x'$  and  $y'$  are along the two orthogonal dimer directions (see Fig. 1(a)). Note that there are four  $\text{RE}^{3+}$  ions within a unit cell (labeled as  $\text{RE}_0, \text{RE}_1, \text{RE}_2, \text{RE}_3$ , respectively in Fig. 1(a)) that are related by the four-fold roto-inversion  $S_4$  about the  $z$  axis. Without loss of generality, we first focus on the  $\text{RE}_1$  sublattice, and then expand our results to the other three. As mentioned above, the point group symmetry of each  $\text{RE}^{3+}$  ion only contains a mirror reflection  $\sigma_v$  with the mirror plane parallel to the corresponding dimer direction, see Fig. 1. The CEF calculations [39] suggest that the quasi-doublet states  $|\psi_{\pm}\rangle$  carry  $A_1$  and  $A_2$  representations of  $\sigma_v$ , respectively:

$$\sigma_v : |\psi_{\pm}\rangle \rightarrow \pm|\psi_{\pm}\rangle.$$

Here we omit the site indices for simplicity. We assume that the magnetism of the system can be understood within this low-energy sector. This two-level subsystem is described by an effective spin-1/2 model. The effective spin-1/2 operators can be constructed as Pauli matrices acting on the two-level system:  $\hat{\sigma}^{\alpha} \equiv \frac{1}{2} \sum_{\mu, \nu=\pm} |\psi_{\mu}\rangle \tau_{\mu\nu}^{\alpha} \langle\psi_{\nu}| = \frac{1}{2} \psi \tau^{\alpha} \psi^{\dagger}$  where  $\psi = (|\psi_{+}\rangle, |\psi_{-}\rangle)^T$  and  $\tau^{\alpha}$  ( $\alpha = 1, 2, 3$ ) are Pauli matrices. Denote  $\mathcal{P} \equiv \psi \psi^{\dagger} = |\psi_{+}\rangle \langle\psi_{+}| + |\psi_{-}\rangle \langle\psi_{-}|$  as the projection operator onto the two-level subspace. For each spin component, the symmetry transformations under the mirror reflection  $\sigma_v$  and time-reversal  $\Theta$  are as follows:

$$\sigma_v : \hat{\sigma}^1 \rightarrow -\hat{\sigma}^1, \hat{\sigma}^2 \rightarrow -\hat{\sigma}^2, \hat{\sigma}^3 \rightarrow \hat{\sigma}^3,$$

$$\Theta : \hat{\sigma}^1 \rightarrow -\hat{\sigma}^1, \hat{\sigma}^2 \rightarrow \hat{\sigma}^2, \hat{\sigma}^3 \rightarrow \hat{\sigma}^3.$$

One sees that both  $\hat{\sigma}^2$  and  $\hat{\sigma}^3$  components are even under time-reversal and therefore behave as electric quadrupoles. Meanwhile,  $\hat{\sigma}^1$  is odd under both time-reversal and the mirror reflection and corresponds to a magnetic dipole within the mirror plane (a pseudovector transforming as  $\mathcal{J}^{x'}$  or  $\mathcal{J}^z$  under crystalline symmetries). This result can be obtained in a more formal way by projecting the total angular momentum  $\mathcal{J}$  onto the two-level subspace  $\hat{\mathbf{j}} = \mathcal{P} \mathcal{J} \mathcal{P}$  and rewrite the dipolar operator as  $\hat{\mathbf{j}} = A \hat{\sigma}^1 \mathbf{n}$ , where  $A$  describes the magnitude of the dipole moment, and  $\mathbf{n}$  is the unit vector representing the direction of the dipole axis. Note that  $\mathcal{J}^{x'}$  and  $\mathcal{J}^z$  transform according to the same representation of the crystalline symmetry. Consequently, the dipole direction  $\mathbf{n}$  cannot be completely determined by symmetry, but depends on microscopic details of crystal field wave functions.

The above discussions are restricted to the  $\text{RE}_1$  ion. As the four RE ions within the unit cell are connected by the four-fold roto-inversion about  $z$  axis, their individual local dipole axes  $\mathbf{n}_i$  should be connected by the four-fold counter-rotation. Therefore, the local dipole axes  $\mathbf{n}_i$  at sublattice  $i$  should have identical out-of-plane component, while their in-plane components follow the directions as shown in Fig. 1. Note that such sublattice-dependent structure of dipole moments makes their coupling to external magnetic field peculiar, and complicates the analysis of magnetization and magnetic susceptibility data, as will be discussed in detail in Sec. III.

### C. Effective Hamiltonian

In this subsection, we derive a generic Hamiltonian based on symmetry analysis. Considering the strongly localized nature of 4f electronic orbitals, we expect the exchange interactions decay rapidly with inter-moment distance. To keep the analysis as concise as possible, here we only give the results for the intra-dimer and nearest-neighbor (NN) inter-dimer interactions. The interaction between further neighboring spins can be derived in a similar way.

We start from derivation of the intra-dimer interactions. The dimer is protected by two mirror reflection symmetries  $\sigma_v$  and  $\sigma'_v$ , with the mirror planes parallel and perpendicular to the dimer directions, respectively (see Fig. 1(a)). The most general form of the intra-dimer interactions can be written as bilinears of effective spin operators:  $H_J = \sum_{\langle\langle ij \rangle\rangle \alpha\beta} J_{ij}^{\alpha\beta} \hat{\sigma}_i^{\alpha} \hat{\sigma}_j^{\beta}$ , where  $J_{ij}^{\alpha\beta}$  refers to the intra-dimer exchange coupling between  $\alpha$  component of the effective spin located at sites  $i$  and the  $\beta$  component of the spin at site  $j$ . Time-reversal symmetry forbids any mixing between dipole and quadrupole moments. This immediately leads to  $J_{ij}^{12} = J_{ij}^{13} = J_{ij}^{21} = J_{ij}^{31} = 0$ . Moreover, the mirror reflection  $\sigma_v$  forbids linear mixing of  $\hat{\sigma}_i^2$  and  $\hat{\sigma}_j^3$  components since they have different parities. As a result,  $J_{ij}^{23} = J_{ij}^{32} = 0$ . Therefore, the intra-dimer interaction simply takes the form of an XYZ model

$$H_J = \sum_{\langle\langle ij \rangle\rangle} J^{11} \hat{\sigma}_i^1 \hat{\sigma}_j^1 + J^{22} \hat{\sigma}_i^2 \hat{\sigma}_j^2 + J^{33} \hat{\sigma}_i^3 \hat{\sigma}_j^3. \quad (1)$$

Note that although the system does not contain any spatial-

inversion symmetries at the center of the dimer, the intra-dimer antisymmetric Dzyaloshinskii-Moriya interaction (DMI) [42, 43] is still disallowed by the spatial and time-reversal symmetries.

Next we consider the NN inter-dimer interaction. The interaction takes the generic bilinear form  $H_J = \sum_{\langle ij \rangle \alpha \beta} J_{ij}^{\alpha \beta} \hat{\sigma}_i^\alpha \hat{\sigma}_j^\beta$ . Time-reversal symmetry also forbids linear mixing between dipole and quadrupole moments:  $J_{ij}^{12} = J_{ij}^{13} = J_{ij}^{21} = J_{ij}^{31} = 0$ . Since there is no other symmetry to further constrain the interactions, the NN interaction takes a more complicated bond-dependent form

$$H_J = \sum_{\langle ij \rangle} (\hat{\sigma}_i^1, \hat{\sigma}_i^2, \hat{\sigma}_i^3) \begin{pmatrix} J^{11} & & \\ & J^{22} & \eta_{ij} J^{23} \\ & \eta_{ij} J^{32} & J^{33} \end{pmatrix} \begin{pmatrix} \hat{\sigma}_j^1 \\ \hat{\sigma}_j^2 \\ \hat{\sigma}_j^3 \end{pmatrix} \quad (2)$$

where  $\langle ij \rangle$  follows the bond direction  $i \rightarrow j$  as shown in Fig. 1(b). The bond dependence of the inter-dimer interactions is taken over by the off-diagonal  $\eta_{ij}$  term, which takes the values 1 and  $-1$  for the red and blue bonds, respectively.

Besides the exchange couplings, we have to consider the effect of crystal field, which causes a splitting  $\Delta$  between the two levels of the quasi-doublet. This can be taken as an intrinsic field acting on the quadrupole component  $\hat{\sigma}^3$  [23, 24]

$$H_\Delta = -\Delta \sum_i \hat{\sigma}_i^3. \quad (3)$$

The total Hamiltonian then takes the following form

$$H = H_{J'} + H_J + H_\Delta. \quad (4)$$

### III. COUPLING TO THE MAGNETIC FIELD

In this section, we discuss the implications of the sublattice-dependent dipole moment structure when coupled to an external magnetic field. Denoting the sublattice index as  $i$  ( $i = 0, 1, 2, 3$  for the four sites within a unit cell), the general form of Zeeman coupling takes the form

$$\begin{aligned} H_B &= -\mu_B g_J \sum_\alpha B^\alpha \sum_{i=0}^3 \hat{j}_i^\alpha \\ &= -\mu_B g_J \sum_\alpha B^\alpha \sum_{i=0}^3 (\mathbf{n}_i \cdot \hat{\mathbf{e}}_\alpha) \hat{j}_i^{\mathbf{n}_i} \\ &= -\mu_B g_J \sum_\alpha B^\alpha \sum_{i=0}^3 (\mathbf{n}_i \cdot \hat{\mathbf{e}}_\alpha) A \hat{\sigma}_i^1. \end{aligned} \quad (5)$$

Here  $B^\alpha$  denotes the applied magnetic field along the  $\alpha$  direction,  $\alpha = x, y, z$  corresponds to the spatial directions where  $x, y$  are obtained from  $x', y'$  by a rotation of  $45^\circ$  about the  $z$  axis.  $g_J$  is the Landé  $g$ -factor,  $\hat{j}_i^\alpha$  is the projection of the total angular momentum  $\mathcal{J}_i^\alpha$  onto the low-energy subspace:

$$\hat{j}_i^\alpha \equiv \mathcal{P}_i \mathcal{J}_i^\alpha \mathcal{P}_i. \quad (6)$$

Given that the effective spin components  $\hat{\sigma}_i^2$  and  $\hat{\sigma}_i^3$  are even under time-reversal, only the dipolar component  $\hat{\sigma}_i^1$  directly couples to the external magnetic field. More interestingly, because the dipole axis direction  $\mathbf{n}_i$  exhibits sublattice dependence, the in-plane and out-of-plane field couples to  $\hat{\sigma}_i^1$  differently. The out-of-plane magnetic field couples to the uniform magnetization of the dipolar spin component  $\hat{\sigma}_0^1 + \hat{\sigma}_1^1 + \hat{\sigma}_2^1 + \hat{\sigma}_3^1$  just like in ordinary magnets, but the in-plane magnetic field turns out to couple to the staggered magnetization of the dipolar moments. For example, the in-plane field  $\mathbf{B} \parallel [100]$  couples to  $\hat{\sigma}_0^1 - \hat{\sigma}_1^1 - \hat{\sigma}_2^1 + \hat{\sigma}_3^1$ . In Tab. I we have listed several more examples on how the field couples to the dipolar moments.

This peculiar coupling of dipole moments to the external magnetic field makes the behavior of magnetic susceptibilities quite different from conventional magnetic materials. At high-temperatures, the magnetic susceptibility per RE site should satisfy the Curie-Weiss (CW) law

$$\chi \approx \frac{C}{T - \Theta_{\text{CW}}}, \quad (7)$$

where  $\Theta_{\text{CW}}$  is the CW temperature and  $C$  is the CW parameter. In Appendix A, we have derived the CW behaviors for different field directions and the results are summarized in Tab. I. As the in-plane and out-of-plane fields couple to different magnetization patterns, the corresponding CW temperatures turns out to reflect interactions along different bonds. This behavior is quite different from ordinary magnets where the in-plane and out-of-plane CW temperatures reflect the magnetic exchanges along corresponding directions. The above results imply that we could extract the values of  $J^{11}$  and  $J'^{11}$  exchange interactions from the experimental susceptibility data. However, the exchange couplings associated with other effective spin components are not available because they reflect interactions among quadrupolar moments which do not directly couple to the external magnetic field.

### IV. PHASE DIAGRAM

Before discussing the numerical phase diagram of the model Eq. (4), we first make a comparison of the generic effective models between the Kramers [41] and non-Kramers systems. The interactions between the non-Kramers local moments are described by an extended XYZ model along both intra- and inter-dimer bonds, which are very much like the case of the Kramers doublets. Therefore, our following discussions on the physical effects of exchange anisotropy will still be applicable to Kramers systems. Meanwhile, there exists substantial differences of non-Kramers systems from the Kramers counterpart, which are reflected in the following two aspects.

First, the physical nature of the local moments differs significantly between Kramers and non-Kramers systems. In Kramers systems, all effective spin components are magnetic dipoles that are linearly coupled to the external magnetic field and their ordering is detectable by neutron diffraction. In contrast, for non-Kramers systems only one component of the effective spin behaves as magnetic dipole, while the

Field direction	Induced magnetization	$C$	$\Theta_{CW}$
[001]	$\mu_B g_J A_{\perp} (\hat{\sigma}_0^1 + \hat{\sigma}_1^1 + \hat{\sigma}_2^1 + \hat{\sigma}_3^1)$	$k_B^{-1} (\mu_B g_J A_{\perp})^2 / 4$	$-k_B^{-1} (4J^{11} + J'^{11}) / 4$
[100]	$\mu_B g_J A_{\parallel} / \sqrt{2} (\hat{\sigma}_0^1 - \hat{\sigma}_1^1 - \hat{\sigma}_2^1 + \hat{\sigma}_3^1)$	$k_B^{-1} (\mu_B g_J A_{\parallel})^2 / 8$	$k_B^{-1} J'^{11} / 4$
[010]	$\mu_B g_J A_{\parallel} / \sqrt{2} (-\hat{\sigma}_0^1 - \hat{\sigma}_1^1 + \hat{\sigma}_2^1 + \hat{\sigma}_3^1)$	$k_B^{-1} (\mu_B g_J A_{\parallel})^2 / 8$	$k_B^{-1} J'^{11} / 4$
[110]	$\mu_B g_J A_{\parallel} (-\hat{\sigma}_1^1 + \hat{\sigma}_3^1)$	$k_B^{-1} (\mu_B g_J A_{\parallel})^2 / 8$	$k_B^{-1} J'^{11} / 4$
$[\bar{1}10]$	$\mu_B g_J A_{\parallel} (-\hat{\sigma}_0^1 + \hat{\sigma}_2^1)$	$k_B^{-1} (\mu_B g_J A_{\parallel})^2 / 8$	$k_B^{-1} J'^{11} / 4$

Table I. Induced magnetization, Curie-Weiss parameter  $C$  and Curie-Weiss temperature  $\Theta_{CW}$  for different field directions. Here  $A_{\perp} \equiv A(\mathbf{n}_i \cdot \hat{\mathbf{e}}_{\perp})$  and  $A_{\parallel} \equiv A(\mathbf{n}_i \cdot \hat{\mathbf{e}}_{\parallel})$  denote the magnitudes of out-of-plane and in-plane dipole components  $\hat{\sigma}^1$ , respectively.

other two are quadrupoles that are invisible to neutrons. If the quadrupole components exhibit some non-vanishing order  $\langle \hat{\sigma}^2 \rangle \neq 0$  or  $\langle \hat{\sigma}^3 \rangle \neq 0$ , such quadrupole ordering would not be quite visible in conventional measurements. This poses an interesting challenge on how to identify these hidden quadrupole ordered phases in experiments. Another difference is that in Kramers systems the crystal field levels exhibit Kramers degeneracy protected by the time reversal symmetry. Meanwhile, for non-Kramers systems there is no such symmetry protection, hence the lowest two crystal field levels have a finite splitting. This splitting is taken into account by an intrinsic field  $H_{\Delta} = -\Delta \sum_i \hat{\sigma}_i^3$  that acts on the quadrupole component  $\hat{\sigma}^3$ . In real materials the magnitude of crystal field splitting are usually non-negligible compared to the exchange interactions, therefore this intrinsic field term must be seriously taken into account.

#### A. Anisotropic XXZ and XYZ model with zero intrinsic field $\Delta = 0$

Previous numerical studies on the SSL magnets are mainly focused on the isotropic Heisenberg model. Given the low symmetry of systems we considered in this work, the effective Hamiltonian Eq. (4) exhibits highly anisotropic interactions with a large number of free parameters. To make our analysis more manageable, we first ignore the intrinsic field  $\Delta = 0$  and begin by exploring the phase diagram in the presence of XXZ anisotropy. Then we investigate the effects of the XYZ anisotropy to the system. Note that the model Eq. (4) at zero intrinsic field limit  $\Delta = 0$  is quite analogous to that of the Kramers system, despite the different physical nature of the effective spin components. So our discussion here is also applicable to the Kramers system. The role of non-zero intrinsic field will be discussed in the next subsection.

For the XXZ model, to simplify our discussions, we assume that the exchange anisotropy  $\delta$  are the same for the intra- and inter-dimer interactions:

$$H = \sum_{\langle\langle ij \rangle\rangle} J' (\delta \hat{\sigma}_i^1 \hat{\sigma}_j^1 + \hat{\sigma}_i^2 \hat{\sigma}_j^2 + \hat{\sigma}_i^3 \hat{\sigma}_j^3) + \sum_{\langle ij \rangle} J (\delta \hat{\sigma}_i^1 \hat{\sigma}_j^1 + \hat{\sigma}_i^2 \hat{\sigma}_j^2 + \hat{\sigma}_i^3 \hat{\sigma}_j^3), \quad (8)$$

where the anisotropy parameter  $\delta$  interpolates between the XY ( $\delta = 0$ ) and Ising limit ( $\delta \rightarrow \infty$ ). This model has a global

U(1) symmetry generated by the global effective-spin rotation of arbitrary angle  $\theta$  respect to the  $\hat{\sigma}^2$ - $\hat{\sigma}^3$  plane. To calculate the phase diagram, we employ the variational optimization of the 16-PESS (Projected Entangled Simplex States) tensor network states [44–46]. In this context, the 16-PESS structure of the SSL incorporates  $U$  and  $S$  tensors [47]. The  $U$  tensor is defined within the plaquettes containing intra-dimer interactions and is connected by the entangled simplex tensor  $S$ . The  $S$  tensor, which does not carry any physical spin degrees of freedom, is introduced to describe the entanglement among the spin clusters. We performed the calculations within a  $2 \times 2$  unit cell, and employed translational symmetry throughout the process. We utilized the corner transfer matrix renormalization group (CTMRG) [48] for infinite network contraction. All results via the variational optimization are obtained by using a bond dimension  $D = 4$  and CTMRG truncation dimension  $\chi = 50$ .

The numerical phase diagram of the XXZ model Eq. (8) is presented in Fig. 3. We find that the dimerized and plaquette phases in the SSL Heisenberg model are still stable against XXZ anisotropy. In the Ising anisotropic case ( $\delta > 1$ ), the AFM phase in the Heisenberg case remains, which is now denoted as the  $\sigma^1$ -AF phase. But for the XY anisotropic case ( $\delta < 1$ ), the ordering of  $\sigma^2$  or  $\sigma^3$  (denoted as  $\sigma^{2,3}$ -AF phase) actually corresponds to an antiferro-quadrupolar (AFQ) order. Specifically, when  $J/J'$  is relatively small, the dimer phase can remain stable throughout the entire parameter space of  $\delta$ . In the  $\delta \rightarrow 0$  limit, we find the dimerized phase undergoes a direct transition to the  $\sigma^{2,3}$ -antiferro-quadrupole (AFQ) phase at  $J/J' = 0.63$ . In the Ising limit ( $\delta \rightarrow \infty$ ) the transition between the dimerized and the  $\sigma^1$ -AF phases occurs at  $J/J' = 0.5$ , consistent with the value of previous theoretical studies [49, 50]. The plaquette phase can remain stable over a certain range of anisotropy before transitioning to the  $\sigma^1$ -AFM or  $\sigma^{2,3}$ -AFQ phase.

In systems corresponding to real materials, the exchange anisotropy is of an extended XYZ form that has even lower symmetry than the above XXZ model, with the global U(1) symmetry explicitly broken. As the generic Hamiltonian Eq. (4) at  $\Delta = 0$  still contains many free parameters, we simplify our discussions by ignoring the off-diagonal interactions, setting  $J^{\alpha\beta} = 0$  for  $\alpha \neq \beta$ . In addition, we fix the relative proportions of the corresponding inter-dimer interactions to match those of the intra-dimer ones, *i.e.*,  $J^{11}/J^{33} = J'^{11}/J'^{33}$  and  $J^{22}/J^{33} = J'^{22}/J'^{33}$ . Since the plaquette phase has the

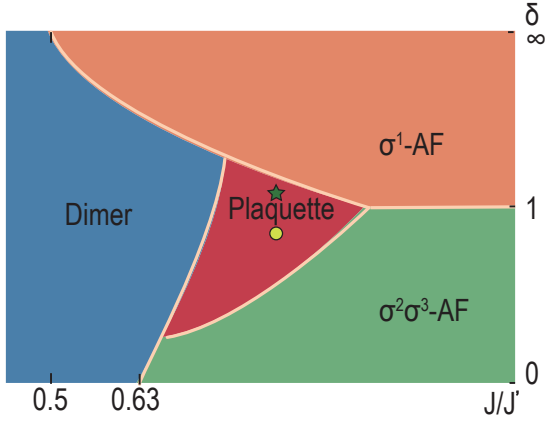


Figure 3. Phase diagram of the antiferromagnetic XXZ model Eq. (8) with zero intrinsic field  $\Delta = 0$ . For non-Kramers systems  $\hat{\sigma}^1$  is a dipole and  $\hat{\sigma}^2$  and  $\hat{\sigma}^3$  are quadrupoles,  $\sigma^1$ -AF corresponds to an AFM state with ordering of the  $\sigma^1$  component, and  $\sigma^2\sigma^3$ -AF corresponds to an AFQ state with ordering of the  $\sigma^{2,3}$  components.

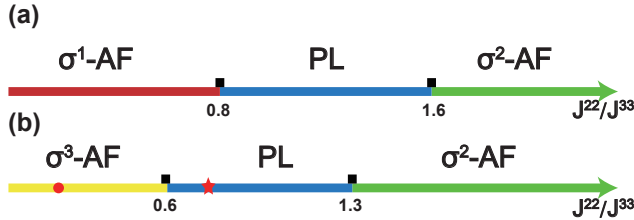


Figure 4. Phase diagrams of the antiferromagnetic XYZ model with zero intrinsic field  $\Delta = 0$ . For non-Kramers systems,  $\hat{\sigma}^1$ -AF is an AFM order, while  $\hat{\sigma}^2$  ( $\hat{\sigma}^3$ )-AF are AFQ orders. (a) Phase diagram with  $J^{22}/J^{33}$  at  $J^{22} = 1$ ,  $J^{11} = 0.816$ ,  $J^{33} = 0.68$ ,  $J'^{11} = 1.2$ ,  $J'^{33} = 1.0$ . The ground state for  $J^{22} = J^{33}$  corresponds to the green star in Fig. 3. (b) Phase diagram with  $J^{22}/J^{33}$  at  $J'^{22} = 1$ ,  $J^{11} = 0.544$ ,  $J^{33} = 0.68$ ,  $J'^{11} = 0.8$ ,  $J'^{33} = 1.0$ . The ground state for  $J^{22} = J^{33}$  corresponds to the yellow circle in Fig. 3.

strongest quantum fluctuations among the four phases of the phase diagram in Fig. 3, we select two representative parameter points within the plaquette phase in the XXZ phase diagram (depicted by the green star and yellow circle in Fig. 3), and calculate the ground-state phase diagram in the presence of finite XYZ anisotropy  $J^{22} \neq J^{33}$ . From the calculated phase diagrams shown in Fig. 4, we find that because of its gapped nature, the plaquette phase remains stable when the XYZ anisotropy is not strong. As the anisotropy further increases, the system ultimately enters to either AFM or AFQ phase depending on the anisotropic factors.

### B. Non-zero intrinsic field $\Delta \neq 0$

Here we focus on the non-Kramers system and investigate the fate of phase diagram under a finite intrinsic field  $\Delta \neq 0$  that acts on the quadrupole effective-spin component  $\hat{\sigma}^3$ . As

the intrinsic field is resulted from single-ion physics of crystal field splitting, in general it should not be negligible compared with the exchange interactions hence must be seriously taken into account. To illustrate the physical effects of  $\Delta$ , we have selected a few representative parameter points (the red circle and star in Fig. 4, for example), such that the zero-field limit  $\Delta = 0$  locate within the dimer, plaquette and AF phases, respectively. To account for the possibility of incommensurate magnetic order when an external field is applied, we perform the calculation by using the density matrix renormalization group (DMRG) algorithm [51, 52] here. The calculation is performed on a  $W \times L$  cylinder with width  $W$  and length  $L$ . Previous works on the Heisenberg model [10, 52] indicates that the minimal width required to realize the plaquette singlet phase is  $W = 6$ . Here, we adopt  $W = 6$  and set the length  $L = 30$ . The bond dimension  $D$  kept is equal to 1024. The calculated phase diagrams versus the intrinsic field  $\Delta$  are shown in Fig. 5, and the corresponding quadrupolar polarization  $M \equiv \frac{1}{N} \sum_i \hat{\sigma}^3$  versus  $\Delta$  curves are shown in Fig. 6.

The evolution of the isotropic Heisenberg system under an external magnetic field has been extensively studied in the context of the  $\text{SrCu}_2(\text{BO}_3)_2$  compound both experimentally [13, 53–57] and numerically [11, 58–61]. The magnetic field induces a rich phase diagram with many fractional magnetization plateau phases, such as  $1/5$ ,  $1/4$ ,  $1/3$ ,  $1/2$  plateaus, reflecting the strong geometric frustration of the SSL. Similarly, for the non-Kramers system with strong spin anisotropy we have also observed complicated evolution of ground states under the intrinsic field  $\Delta$ .

For the plaquette and AFQ phases at zero  $\Delta$ , the field-induced behaviors are qualitatively quite similar as shown in Fig. 5(a) and (b). As both phases are gapped, they are stable against small fields  $\Delta$ . With increasing  $\Delta$ , the plaquette/AFQ phases become unstable, developing coexisting AFQ

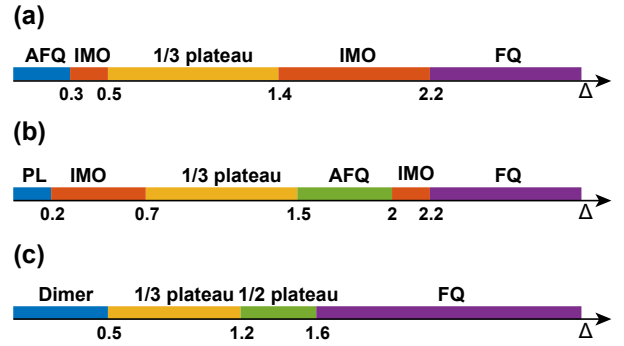


Figure 5. Phase diagrams of the non-Kramers model Eq. (4) versus the intrinsic field  $\Delta$ . The parameters are chosen such that the zero-field ground states are (a) the AFQ phase with  $J^{11} = 0.544$ ,  $J^{22} = 0.136$ ,  $J^{33} = 0.68$ ,  $J'^{11} = 0.8$ ,  $J'^{22} = 0.2$ ,  $J'^{33} = 1.0$ ; (b) the plaquette phase, with  $J^{11} = 0.544$ ,  $J^{22} = 0.51$ ,  $J^{33} = 0.68$ ,  $J'^{11} = 0.8$ ,  $J'^{22} = 0.75$ ,  $J'^{33} = 1.0$ ; and (c) the dimerized phase with  $J^{11} = 0.4$ ,  $J^{22} = 0.3$ ,  $J^{33} = 0.5$ ,  $J'^{11} = 0.8$ ,  $J'^{22} = 0.6$ ,  $J'^{33} = 1.0$ , respectively. FQ, AFQ, and IMO refer to ferro-quadrupolar order, antiferro-quadrupolar order, and intertwined multipolar order, respectively.

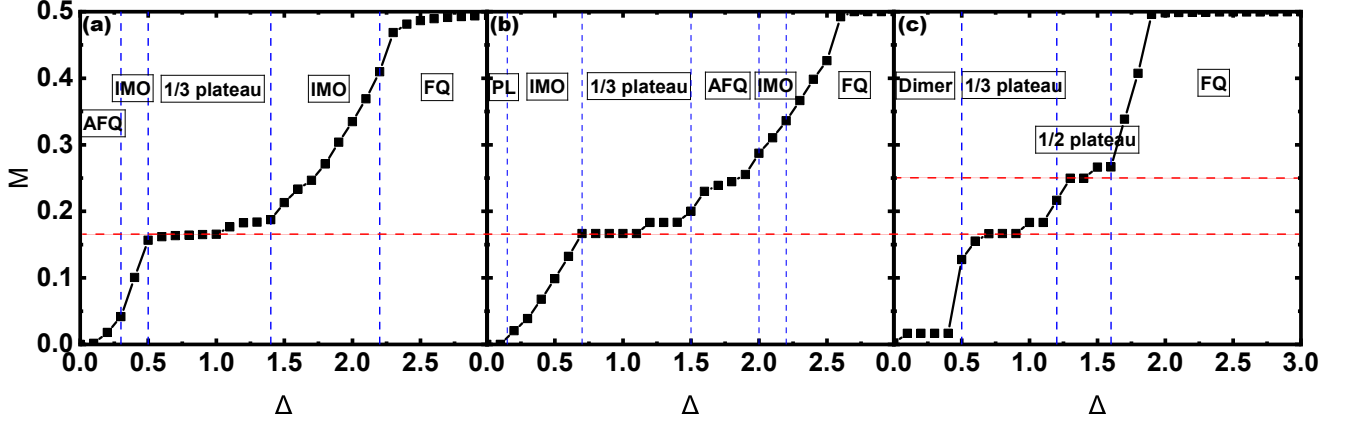


Figure 6. Quadrupole polarization  $M$  versus the intrinsic field  $\Delta$ . The parameters are chosen as same as those in Fig. 5. The dashed line indicates  $M$  reaches  $1/3$  and  $1/2$  of its saturated value.

and AFM orders which is denoted as an “intertwined multipolar order” (IMO) [22, 24]. Our DMRG results show that the ordering vectors of both dipole and quadrupole components  $\hat{\sigma}^1$  and  $\hat{\sigma}^3$  are incommensurate. Then it enters a peculiar type of  $3 \times 1$  AFQ with approximate  $1/3$  quadrupole polarization. This phase is the counterpart of the “ $1/3$ -plateau” phase of the Heisenberg system [54, 59], and its nature will be discussed in detail in the next subsection. After across another IMO phase, the system eventually becomes completely polarized under sufficiently large  $\Delta$ . On the other hand, starting from the dimerized state, the in-field phase diagrams is much simpler. The system subsequently enters the “ $1/3$ -plateau” phase and a “ $1/2$ -plateau” phase, before fully polarized by the intrinsic field. In the “ $1/2$ -plateau” plateau phase, the spin configuration is a defected FQ state. The magnitude of the magnetic moments exhibits a distribution with a  $(\pi, \pi)$  periodicity. The real-space pattern of effective spins of this state is shown in Fig. 7: In one unit cell, one dimer forms a spin singlet state, while the effective spins of the other dimer are polarized by the intrinsic field and form an FQ order.

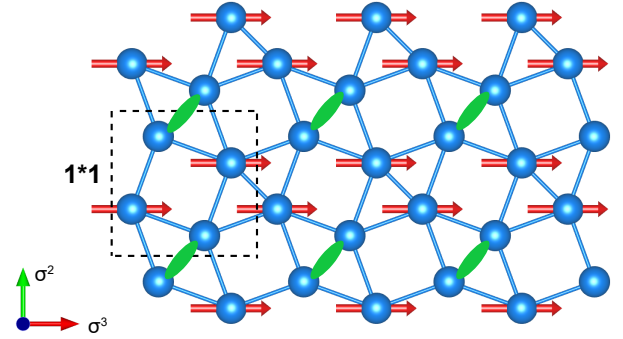


Figure 7. Effective-spin configuration of the  $1/2$ -“plateau” phase. The green bond represents a singlet dimer and the red arrow indicates the FQ order of effective spins induced by the intrinsic field.

### C. Hidden “ $1/3$ -plateau” phase

In the phase diagrams of Fig. 5 we observe wide existence of the “ $1/3$ -plateau” phase stabilized by the intrinsic field  $\Delta$ . Its effective spin structure is identical to that of the Heisenberg systems: the spins form a  $3 \times 1$  superstructure (see Fig. 8) where every third dimer forms a triplet that aligns along the field direction while in the remaining dimers two spins are alternatively aligned and anti-aligned along the field. This state has six-fold degeneracy that breaks both the  $\mathbb{Z}_3$  translational and  $\mathbb{C}_2$  rotational symmetries. In the specific heat measurements, such a symmetry breaking could be reflected as some divergence behaviors upon varying temperatures. However, notice that such ordering occurs purely in the quadrupolar sector, hence is not directly visible from the conventional experimental probes such as neutron diffraction, which corresponds to one type of hidden order. Moreover, the intrinsic

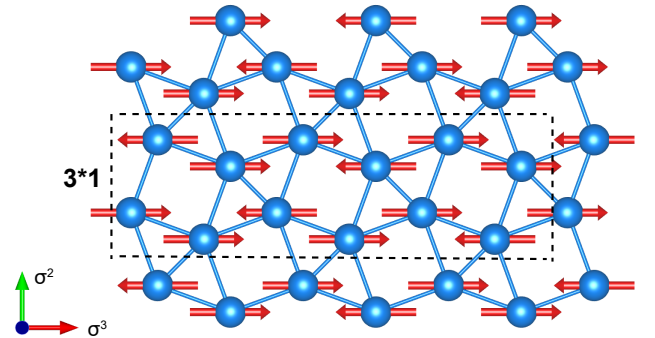


Figure 8. Effective-spin configuration of the  $1/3$ -“plateau” phase.

field comes from the crystal field splitting which can be tuned by either applying external pressure or chemical doping. But in either case the tunability is very limited. These difficulties pose an important question on how to identify this hidden quadrupolar ordered phase in experiments.

As proposed in Refs. [22, 62], the information of quadrupole orderings can be indirectly reflected in dynamical measurements such as inelastic neutron scattering. This is due to the non-commutative relation between the dipolar and the quadrupolar components. As neutron spins only couple to the magnetic dipolar component  $\hat{\sigma}^1$  at the linear order, in inelastic neutron scattering what is measured is the dipole-dipole correlation

$$S^{11}(\mathbf{q}, \omega) = \frac{1}{2\pi N} \sum_{ij} \int_{-\infty}^{+\infty} dt e^{i\mathbf{q}\cdot(\mathbf{r}_i - \mathbf{r}_j) - i\omega t} \langle \hat{\sigma}_i^1(0) \hat{\sigma}_j^1(t) \rangle. \quad (9)$$

Fortunately, this dynamical dipole-dipole correlation is able to reflect the dynamics of the  $\langle \hat{\sigma}^3 \rangle \neq 0$  quadrupolar order. When neutron spins measure the  $\hat{\sigma}^1$  dipolar moment, they induce spin flip events on the quadrupolar moments, thereby creating coherent quadrupole-wave excitations. These excitations carry information about the underlying quadrupolar orderings. Thus, although quadrupolar ordering itself cannot be observed in experiments, their dynamical excitations can be indirectly probed.

Here we use the linear spin-wave theory to calculate the dynamical spin structure factor  $S^{11}(\mathbf{q}, \omega)$  which can be directly measured in inelastic neutron scattering experiments. The spin-wave calculation is performed with the SUNNY package [63], and the excitation spectra are shown in Fig. 9. In the spectra, we observe many branches of spin-wave dispersion, consistent with the large magnetic supercell structure of the “1/3-plateau” phase. All spin-wave branches are rather flat, indicating that such phase is rather classical with significantly suppressed quantum fluctuations. This  $3 \times 1$  structure is further reflected by the band folding along the  $[0 \ 1/2 \ 0]$ - $[1 \ 1/2 \ 0]$  line, indicating a period-of-three structure along the  $[100]$  direction. Moreover, the excitations become two-fold degenerate along the  $[0 \ 1/2 \ 0]$ - $[1 \ 1/2 \ 0]$  line, with its physical reason may be accounted by symmetries.

## V. DISCUSSIONS AND CONCLUSIONS

In this paper, we propose and study a generic spin model that describes the interaction between the non-Kramers local moments relevant for the Shastry-Sutherland lattice rare-earth magnets. We point out that the local moments consist of both magnetic dipolar and quadrupolar components. The effective model turns out to be an extended XYZ model with an intrinsic field that accounts for the crystal field splitting. We discuss physical effects of the XXZ and XYZ exchange anisotropy, as well as the intrinsic field  $\Delta$  to the system. Moreover, in the phase diagram we find wide existence of pure quadrupolar orders that are invisible in conventional experimental probes. We focus on the “1/3-plateau” pure quadrupolar order and discuss its experimental signatures in dynamical excitations.

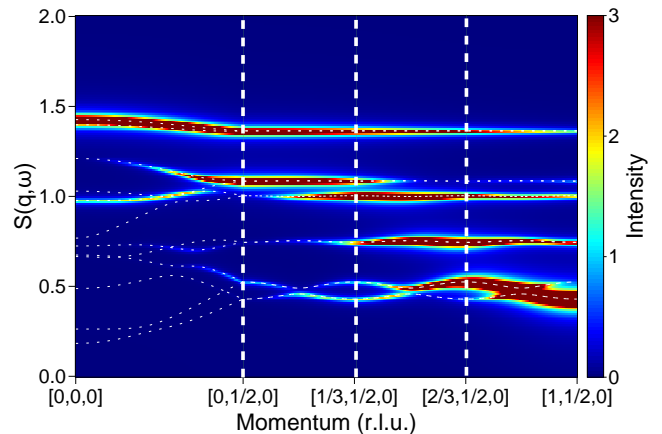


Figure 9. Dynamical structural factor  $S^{11}(\mathbf{q}, \omega)$  for the “1/3-plateau” phase. Spin-wave dispersions are marked by thin dashed lines. The model parameters are  $J^{11} = 0.544$ ,  $J^{22} = 0.136$ ,  $J^{33} = 0.68$ ,  $J^{11} = 0.8$ ,  $J^{22} = 0.2$ ,  $J^{33} = 1.0$ ,  $\Delta = 0.9$ .

For the Shastry-Sutherland lattice, there are four spins per unit cell, hence the Lieb-Shultz-Mattis theorem [64–67] do not apply to such systems. Moreover, crystal field splitting can induce a finite intrinsic field to the system. Therefore, absence of ordering signal in experiments does not necessarily imply a non-trivial spin liquid ground state, but can also be trivial quantum paramagnets such as dimer singlet and the  $\hat{\sigma}^3$ -polarized state. Therefore, more experimental probes such as Raman, X-ray scattering, neutron scattering and thermal conductivity measurements, are needed to identify a possible spin liquid state.

Here we discuss the relevance of our results with the non-Kramers Shastry-Sutherland magnets  $\text{Pr}_2\text{Be}_2\text{GeO}_7$  and  $\text{Pr}_2\text{Ga}_2\text{BeO}_7$ . For  $\text{Pr}_2\text{Be}_2\text{GeO}_7$ , experiments find that the system does not show any signatures of long-range magnetic ordering at temperatures as low as 0.08 K, while the AC susceptibility reveal a dynamic spin-freezing behavior below  $\sim 0.22$  K. These experimental signatures indicate strong frustration of this system. However, from the Curie-Weiss temperatures  $\Theta_{\perp} = -0.33$  K and  $\Theta_{\parallel} = -5.13$  K in the experiment, we extract the exchange coupling  $J^{11} \sim 5.46$  K and  $J^{11} \sim -20.52$  K, which is frustration-free in the dipole sector  $\hat{\sigma}^1$ . Similar situations are also found in  $\text{Pr}_2\text{Ga}_2\text{BeO}_7$ . Thermodynamics,  $\mu\text{SR}$  and neutron measurements indicate absence of local moment ordering down to very low temperatures. Moreover, a finite  $\kappa/T$  is observed, suggesting the presence of fermionic spinons at low energies. While these experimental signatures also suggest strong frustration, the dipolar exchange couplings extracted from the susceptibility of this material are found to be  $J^{11} \sim 41.3$  K and  $J^{11} \sim -85.4$  K, which also lacks frustration in the dipole sector. To account for the experiments, it is essential to look into the dynamical frustration effects on the quadrupole sector in more detail, such as the XYZ anisotropy and the inter-dimer  $\Gamma$  and/or Dzyaloshinskii-Moriya type quadrupole-quadrupole interactions ( $H_{\Gamma} \equiv \Gamma \sum_{\langle ij \rangle} \eta_{ij} (\hat{\sigma}_i^2 \hat{\sigma}_j^3 + \hat{\sigma}_i^3 \hat{\sigma}_j^2)$ ) and  $H_{DM} \equiv D \sum_{\langle ij \rangle} \eta_{ij} (\hat{\sigma}_i^2 \hat{\sigma}_j^3 - \hat{\sigma}_i^3 \hat{\sigma}_j^2)$ ) that are present in the ef-



fective model in Eq. (4). Including these terms further complicates the model, and we defer the study of the effects of them in a future work, and we defer the study of the effects of them in a future work. Last but not least, more experimental probes, in particular dynamical spectroscopic measurements, are highly demanded to gain more insight into the nature of ground states of these systems.

### ACKNOWLEDGMENTS

We thank Haidong Zhou, Xuefeng Sun and Jie Ma for useful discussions. This work is supported by the National Key R&D Program of China (Grant No.2023YFA1406500), and the National Science Foundation of China (Grant Nos.12334008 and 12174441). This paper is an outcome of ‘‘Quantum Phase Transition in Low-Dimensional Frustrated Systems’’ (RUC24QSDL038), funded by the ‘‘Qiusi Academic - Dongliang’’ Talent Cultivation Project at Renmin University of China in 2024.

### Appendix A: Curie-Weiss behaviors for non-Kramers systems

In the following we analyze the high-temperature behavior of magnetic susceptibilities in detail. For simplicity here we only consider four RE sublattices within a unit cell, where the RE<sub>*i*</sub> site are labeled by *i* (*i* = 0, 1, 2, 3).

We first consider the out-of-plane magnetic field:

$$H_{[001]} = -\mu_B g_J A_{\perp} B^{[001]} (\hat{\sigma}_0^1 + \hat{\sigma}_1^1 + \hat{\sigma}_2^1 + \hat{\sigma}_3^1). \quad (\text{A1})$$

The out-of-plane magnetic field  $B^{[001]}$  induces a uniform magnetization  $m = \langle \hat{\sigma}_i^1 \rangle$  at each site *i*. This magnetization can be regarded as the combined effect of the external magnetic field and the internal exchange field:

$$m = \chi_p (\mu_B g_J A_{\perp} B^{[001]} + B_{exc}), \quad (\text{A2})$$

where  $\chi_p = (4k_B T)^{-1}$  is the Curie paramagnetic susceptibility,  $B_{exc} = -(4J^{11} + J'^{11})m$  is the exchange field. From the above

relation we obtain

$$m = \frac{\chi_p \mu_B g_J A_{\perp}}{1 + \chi_p (4J^{11} + J'^{11})} B^{[001]}. \quad (\text{A3})$$

The high-temperature magnetic susceptibility per RE site satisfies the Curie-Weiss relation

$$\chi^{[001]} \approx \frac{C}{T - \Theta_{CW}}, \quad (\text{A4})$$

with  $C = k_B^{-1} (\mu_B g_J A_{\perp})^2 / 4$  and  $\Theta_{CW} = -k_B^{-1} (4J^{11} + J'^{11}) / 4$ .

Then we consider the effect of the in-plane magnetic field. We first consider that the field is along the [100] direction.

$$H_{[100]} = -\mu_B g_J A_{\parallel} B^{[100]} / \sqrt{2} (\hat{\sigma}_0^1 - \hat{\sigma}_1^1 - \hat{\sigma}_2^1 + \hat{\sigma}_3^1), \quad (\text{A5})$$

which induces a staggered magnetization, say,  $m$  on RE<sub>1</sub> and RE<sub>2</sub> sublattices, and  $-m$  on RE<sub>0</sub> and RE<sub>3</sub> ones. The formation of the moment is due to the combined effect of the external magnetic field and the internal exchange field:

$$m = \langle \hat{\sigma}_1^1 \rangle = \chi_p (\mu_B g_J A_{\parallel} B^{[100]} / \sqrt{2} + B_{exc}), \quad (\text{A6})$$

where the exchange field  $B_{exc} = J'^{11}m$ . From the above relation we can obtain

$$m = \frac{\chi_p \mu_B g_J A_{\parallel} / \sqrt{2}}{1 - \chi_p J'^{11}} B^{[100]}. \quad (\text{A7})$$

The corresponding Curie-Weiss parameter and Curie-Weiss temperature can then be obtained as  $C = k_B^{-1} (\mu_B g_J A_{\parallel})^2 / 8$  and  $\Theta_{CW} = k_B^{-1} J'^{11} / 4$ .

At least we consider that the field is applied along the [110] direction. The Zeeman coupling becomes:

$$H_{[110]} = -\mu_B g_J A_{\parallel} B^{[110]} (\hat{\sigma}_3^1 - \hat{\sigma}_1^1). \quad (\text{A8})$$

The applied magnetic field induces the staggered magnetization  $m$  at RE<sub>3</sub> site and  $-m$  at RE<sub>1</sub> sites respectively, while it does not couple to the moments of RE<sub>0</sub> and RE<sub>2</sub>. The corresponding Curie-Weiss parameters are  $C = k_B^{-1} (\mu_B g_J A_{\parallel})^2 / 8$  and  $\Theta_{CW} = k_B^{-1} J'^{11} / 4$ , which are identical to those for the [100] field.

[1] C. Lacroix, P. Mendels, and F. Mila, *Introduction to frustrated magnetism: materials, experiments, theory*, Vol. 164 (Springer Science & Business Media, 2011).  
[2] L. Savary and L. Balents, Quantum spin liquids: a review, *Rep. Prog. Phys.* **80**, 016502 (2016).  
[3] L. Balents, Spin liquids in frustrated magnets, *Nature* **464**, 199 (2010).  
[4] B. S. Shastry and B. Sutherland, Exact ground state of a quantum mechanical antiferromagnet, *Physica B+ C* **108**, 1069 (1981).  
[5] S. Miyahara and K. Ueda, Exact dimer ground state of the two dimensional Heisenberg spin system SrCu<sub>2</sub>(BO<sub>3</sub>)<sub>2</sub>, *Phys. Rev. Lett.* **82**, 3701 (1999).

[6] J. Guo, G. Sun, B. Zhao, L. Wang, W. Hong, V. A. Sidorov, N. Ma, Q. Wu, S. Li, Z. Y. Meng, *et al.*, Quantum phases of SrCu<sub>2</sub>(BO<sub>3</sub>)<sub>2</sub> from high-pressure thermodynamics, *Phys. Rev. Lett.* **124**, 206602 (2020).  
[7] S. Haravifard, D. Graf, A. Feiguin, C. Batista, J. Lang, D. Silevitch, G. Srajer, B. Gaulin, H. Dabkowska, and T. Rosenbaum, Crystallization of spin superlattices with pressure and field in the layered magnet SrCu<sub>2</sub>(BO<sub>3</sub>)<sub>2</sub>, *Nat. Commun.* **7**, 11956 (2016).  
[8] Y. Cui, L. Liu, H. Lin, K.-H. Wu, W. Hong, X. Liu, C. Li, Z. Hu, N. Xi, S. Li, *et al.*, Proximate deconfined quantum critical point in SrCu<sub>2</sub>(BO<sub>3</sub>)<sub>2</sub>, *Science* **380**, 1179 (2023).  
[9] M. Zayed, C. Ruegg, J. Larrea J, A. Lauchli, C. Panagopou-

- los, S. Saxena, M. Ellerby, D. McMorrow, T. Strässle, S. Klotz, *et al.*, 4-spin plaquette singlet state in the Shastry–Sutherland compound  $\text{SrCu}_2(\text{BO}_3)_2$ , *Nat. Phys.* **13**, 962 (2017).
- [10] J. Y. Lee, Y.-Z. You, S. Sachdev, and A. Vishwanath, Signatures of a deconfined phase transition on the Shastry-Sutherland lattice: Applications to quantum critical  $\text{SrCu}_2(\text{BO}_3)_2$ , *Phys. Rev. X* **9**, 041037 (2019).
- [11] J. Dorier, K. Schmidt, and F. Mila, Theory of magnetization plateaux in the Shastry-Sutherland model, *Phys. Rev. Lett.* **101**, 250402 (2008).
- [12] T. Momoi and K. Totsuka, Magnetization plateaus of the Shastry-Sutherland model for  $\text{SrCu}_2(\text{BO}_3)_2$ : Spin-density wave, supersolid, and bound states, *Phys. Rev. B* **62**, 15067 (2000).
- [13] T. Nomura, P. Corboz, A. Miyata, S. Zherlitsyn, Y. Ishii, Y. Kohama, Y. Matsuda, A. Ikeda, C. Zhong, H. Kageyama, *et al.*, Unveiling new quantum phases in the Shastry-Sutherland compound  $\text{SrCu}_2(\text{BO}_3)_2$  up to the saturation magnetic field, *Nat. Commun.* **14**, 3769 (2023).
- [14] Y. Zhou, K. Kanoda, and T.-K. Ng, Quantum spin liquid states, *Rev. Mod. Phys.* **89**, 025003 (2017).
- [15] C. Broholm, R. Cava, S. Kivelson, D. Nocera, M. Norman, and T. Senthil, Quantum spin liquids, *Science* **367**, eaay0668 (2020).
- [16] H. Takagi, T. Takayama, G. Jackeli, G. Khaliullin, and S. E. Nagler, Concept and realization of Kitaev quantum spin liquids, *Nat. Rev. Phys.* **1**, 264 (2019).
- [17] S. Trebst and C. Hickey, Kitaev materials, *Phys. Rep.* **950**, 1 (2022).
- [18] A. Kitaev, Anyons in an exactly solved model and beyond, *Ann. Phys.-new. York.* **321**, 2 (2006), January Special Issue.
- [19] A. M. Hallas, J. Gaudet, and B. D. Gaulin, Experimental insights into ground-state selection of quantum XY pyrochlores, *Annu. Rev. Condens. Ma. P.* **9**, 105 (2018).
- [20] S. T. Bramwell and M. J. Gingras, Spin ice state in frustrated magnetic pyrochlore materials, *Science* **294**, 1495 (2001).
- [21] Y. Li, P. Gegenwart, and A. A. Tsirlin, Spin liquids in geometrically perfect triangular antiferromagnets, *J. Phys.: Condens. Matter* **32**, 224004 (2020).
- [22] C. Liu, Y.-D. Li, and G. Chen, Selective measurements of intertwined multipolar orders: non-Kramers doublets on a triangular lattice, *Phys. Rev. B* **98**, 045119 (2018).
- [23] C. Liu, C.-J. Huang, and G. Chen, Intrinsic quantum Ising model on a triangular lattice magnet  $\text{TmMgGaO}_4$ , *Phys. Rev. Research* **2**, 043013 (2020).
- [24] Y. Shen, C. Liu, Y. Qin, S. Shen, Y.-D. Li, R. Bewley, A. Schneidewind, G. Chen, and J. Zhao, Intertwined dipolar and multipolar order in the triangular-lattice magnet  $\text{TmMgGaO}_4$ , *Nat. Commun.* **10**, 4530 (2019).
- [25] L. Savary and T. Senthil, Probing hidden orders with resonant inelastic X-ray scattering, *arXiv preprint arXiv:1506.04752* (2015).
- [26] M. Song, K. Cho, J. Lee, and B. Cho, Abnormal field-dependence of magnetocaloric effect in  $\text{ErB}_4$  and  $\text{TmB}_4$ , *AIP Adv.* **10** (2020).
- [27] D. Lancon, V. Scagnoli, U. Staub, O. Petrenko, M. Ciomaga Hatnean, E. Canévet, R. Sibille, S. Francoual, J. R. Mardegan, K. Beauvois, *et al.*, Evolution of field-induced metastable phases in the Shastry-Sutherland lattice magnet  $\text{TmB}_4$ , *Phys. Rev. B* **102**, 060407 (2020).
- [28] J. Nagl, D. Flavián, S. Hayashida, K. Y. Povarov, M. Yan, N. Murai, S. Ohira-Kawamura, G. Simutis, T. J. Hicken, H. Luetkens, *et al.*, Excitation spectrum and spin Hamiltonian of the frustrated quantum Ising magnet  $\text{Pr}_3\text{BWO}_9$ , *Phys. Rev. Research* **6**, 023267 (2024).
- [29] M. Ashtar, J. Guo, Z. Wan, Y. Wang, G. Gong, Y. Liu, Y. Su, and Z. Tian, A new family of disorder-free rare-earth-based kagome lattice magnets: Structure and magnetic characterizations of  $\text{Re}_3\text{BWO}_9$  (Re= Pr, Nd, Gd–Ho) boratotungstates, *Inorg. Chem.* **59**, 5368 (2020).
- [30] T. Verkholyak and J. Strecka, Fractional magnetization plateaux of a spin-1/2 Heisenberg model on the Shastry-Sutherland lattice: effect of quantum XY interdimer coupling, *SciPost Phys.* **12**, 056 (2022).
- [31] L. Regeciová and P. Farkašovsky, Magnetocaloric effect in the Ising model with RKKY interaction on the Shastry–Sutherland lattice, *Solid State Commun.* **371**, 115251 (2023).
- [32] T. Muto, K. Kobayashi, T. Goto, A. Oosawa, S. Yoshii, T. Sasaki, N. Kobayashi, S. Michimura, F. Iga, and T. Takabatake, 11B-NMR study on Shastry-Sutherland system  $\text{TbB}_4$ , in *J Phys: Conf. Series*, Vol. 400 (IOP Publishing, 2012) p. 032059.
- [33] Y. Ishii, G. Sala, M. B. Stone, V. O. Garlea, S. Calder, J. Chen, H. K. Yoshida, S. Fukuoka, J. Yan, C. dela Cruz, *et al.*, Magnetic properties of the Shastry-Sutherland lattice material  $\text{BaNd}_2\text{ZnO}_5$ , *Phys. Rev. Materials* **5**, 064418 (2021).
- [34] Y. Ishii, J. Chen, H. K. Yoshida, M. Oda, A. D. Christianson, and K. Yamaura, High-pressure synthesis, crystal structure, and magnetic properties of the Shastry-Sutherland-lattice oxides  $\text{BaLn}_2\text{ZnO}_5$  (Ln= Pr, Sm, Eu), *J. Solid State Chem.* **289**, 121489 (2020).
- [35] M. Ashtar, Y. Bai, L. Xu, Z. Wan, Z. Wei, Y. Liu, M. A. Marwat, and Z. Tian, Structure and magnetic properties of melilite-type compounds  $\text{RE}_2\text{Be}_2\text{GeO}_7$  (RE= Pr, Nd, Gd–Yb) with rare-earth ions on Shastry–Sutherland lattice, *Inorg. Chem.* **60**, 3626 (2021).
- [36] A. Brassington, G. Sala, A. Kolesnikov, K. Taddei, Y. Wu, E. Choi, H. Wang, W. Xie, J. Ma, H. Zhou, *et al.*, Magnetic properties of the quasi-XY Shastry-Sutherland magnet  $\text{Er}_2\text{Be}_2\text{SiO}_7$ , *arXiv preprint arXiv:2405.08230* (2024).
- [37] A. Brassington, Q. Huang, A. Aczel, and H. Zhou, Synthesis and magnetic properties of the Shastry-Sutherland family  $\text{R}_2\text{Be}_2\text{SiO}_7$  (R= Nd, Sm, Gd–Yb), *Phys. Rev. Materials* **8**, 014005 (2024).
- [38] L. Yadav, A. Rufino, R. Bag, A. I. Kolesnikov, V. O. Garlea, D. Graf, F. Mila, S. Haravifard, *et al.*, Observation of unprecedented fractional magnetization plateaux in a new Shastry-Sutherland Ising compound, *arXiv preprint arXiv:2405.12405* (2024).
- [39] N. Li, A. Brassington, M. Shu, Y. Wang, H. Liang, Q. Li, X. Zhao, P. Baker, H. Kikuchi, T. Masuda, *et al.*, Spinons in a new Shastry-Sutherland lattice magnet  $\text{Pr}_2\text{Ga}_2\text{BeO}_7$ , *arXiv preprint arXiv:2405.13628* (2024).
- [40] A. Liu, F. Song, Y. Cao, H. Ge, H. Bu, J. Zhou, Y. Qin, Q. Zeng, J. Li, L. Ling, *et al.*, Distinct magnetic ground states in Shastry-Sutherland lattice materials:  $\text{Pr}_2\text{Be}_2\text{GeO}_7$  versus  $\text{Nd}_2\text{Be}_2\text{GeO}_7$ , *Phys. Rev. B* **109**, 184413 (2024).
- [41] C. Liu, G. Duan, and R. Yu, Theory of rare-earth kramers magnets on a shastry-sutherland lattice: dimer phases in presence of strong spin-orbit coupling (2024), [arXiv:2412.00757 \[cond-mat.str-el\]](https://arxiv.org/abs/2412.00757).
- [42] I. Dzyaloshinsky, A thermodynamic theory of “weak” ferromagnetism of antiferromagnetics, *J. Phys. Chem. Solids* **4**, 241 (1958).
- [43] T. Moriya, Anisotropic superexchange interaction and weak ferromagnetism, *Phys. Rev.* **120**, 91 (1960).
- [44] B.-B. Chen, Y. Gao, Y.-B. Guo, Y. Liu, H.-H. Zhao, H.-J. Liao, L. Wang, T. Xiang, W. Li, and Z. Xie, Automatic differentiation

- for second renormalization of tensor networks, *Phys. Rev. B* **101**, 220409 (2020).
- [45] H.-J. Liao, J.-G. Liu, L. Wang, and T. Xiang, Differentiable programming tensor networks, *Phys. Rev. X* **9**, 031041 (2019).
- [46] B. Ponsioen, F. F. Assaad, and P. Corboz, Automatic differentiation applied to excitations with projected entangled pair states, *SciPost Phys.* **12**, 006 (2022).
- [47] N. Xi, H. Chen, Z. Xie, and R. Yu, Plaquette valence bond solid to antiferromagnet transition and deconfined quantum critical point of the Shastry-Sutherland model, *Phys. Rev. B* **107**, L220408 (2023).
- [48] P. Corboz, T. M. Rice, and M. Troyer, Competing states in the t-J model: Uniform d-wave state versus stripe state, *Phys. Rev. Lett.* **113**, 046402 (2014).
- [49] P. Kairys, A. D. King, I. Ozfidan, K. Boothby, J. Raymond, A. Banerjee, and T. S. Humble, Simulating the Shastry-Sutherland Ising model using quantum annealing, *PRX Quantum* **1**, 020320 (2020).
- [50] T. Verkholyak, J. Strečka, F. Mila, and K. P. Schmidt, Exact ground states of a spin-1/2 Ising-Heisenberg model on the Shastry-Sutherland lattice in a magnetic field, *Phys. Rev. B* **90**, 134413 (2014).
- [51] E. M. Stoudenmire and S. R. White, Studying two-dimensional systems with the density matrix renormalization group, *Annu. Rev. Condens. Matter Phys.* **3**, 111 (2012).
- [52] J. Wang, H. Li, N. Xi, Y. Gao, Q.-B. Yan, W. Li, and G. Su, Plaquette singlet transition, magnetic barocaloric effect, and spin supersolidity in the Shastry-Sutherland model, *Phys. Rev. Lett.* **131**, 116702 (2023).
- [53] H. Kageyama, K. Yoshimura, R. Stern, N. Mushnikov, K. Onizuka, M. Kato, K. Kosuge, C. Slichter, T. Goto, and Y. Ueda, Exact dimer ground state and quantized magnetization plateaus in the two-dimensional spin system  $\text{SrCu}_2(\text{BO}_3)_2$ , *Phys. Rev. Lett.* **82**, 3168 (1999).
- [54] K. Onizuka, H. Kageyama, Y. Narumi, K. Kindo, Y. Ueda, and T. Goto, 1/3 magnetization plateau in  $\text{SrCu}_2(\text{BO}_3)_2$  - stripe order of excited triplets, *J. Phys. Soc. Jpn.* **69**, 1016 (2000).
- [55] M. Takigawa, K. Kodama, M. Horvatić, C. Berthier, H. Kageyama, Y. Ueda, S. Miyahara, F. Becca, and F. Mila, The 18-magnetization plateau state in the 2D quantum antiferromagnet  $\text{SrCu}_2(\text{BO}_3)_2$ : spin superstructure, phase transition, and spin dynamics studied by high-field NMR, *Physica B* **346**, 27 (2004).
- [56] F. Levy, I. Sheikin, C. Berthier, M. Horvatić, M. Takigawa, H. Kageyama, T. Waki, and Y. Ueda, Field dependence of the quantum ground state in the Shastry-Sutherland system  $\text{SrCu}_2(\text{BO}_3)_2$ , *Europhys. Lett.* **81**, 67004 (2008).
- [57] M. Jaime, R. Daou, S. A. Crooker, F. Weickert, A. Uchida, A. E. Feiguin, C. D. Batista, H. A. Dabkowska, and B. D. Gaulin, Magnetostriction and magnetic texture to 100.75 tesla in frustrated  $\text{SrCu}_2(\text{BO}_3)_2$ , *Proc. Natl. Acad. Sci.* **109**, 12404 (2012).
- [58] E. Müller-Hartmann, R. R. Singh, C. Knetter, and G. S. Uhrig, Exact demonstration of magnetization plateaus and first-order dimer-Néel phase transitions in a modified Shastry-Sutherland model for  $\text{SrCu}_2(\text{BO}_3)_2$ , *Phys. Rev. Lett.* **84**, 1808 (2000).
- [59] Z. Shi, S. Dissanayake, P. Corboz, W. Steinhardt, D. Graf, D. Silevitch, H. A. Dabkowska, T. Rosenbaum, F. Mila, and S. Haravifard, Discovery of quantum phases in the Shastry-Sutherland compound  $\text{SrCu}_2(\text{BO}_3)_2$  under extreme conditions of field and pressure, *Nat. Commun.* **13**, 2301 (2022).
- [60] P. Corboz and F. Mila, Crystals of bound states in the magnetization plateaus of the Shastry-Sutherland model, *Phys. Rev. Lett.* **112**, 147203 (2014).
- [61] W. Huang, L. Huo, J. Feng, Z. Yan, X. Jia, X. Gao, M. Qin, and J.-M. Liu, Dynamic magnetization process in the frustrated Shastry-Sutherland system  $\text{TmB}_4$ , *Europhys. Lett.* **102**, 37005 (2013).
- [62] Y.-D. Li, X. Wang, and G. Chen, Hidden multipolar orders of dipole-octupole doublets on a triangular lattice, *Phys. Rev. B* **94**, 201114 (2016).
- [63] Sunny suite, <https://github.com/SunnySuite/Sunny.jl>.
- [64] H. Watanabe, H. C. Po, A. Vishwanath, and M. Zaletel, Filling constraints for spin-orbit coupled insulators in symmorphic and nonsymmorphic crystals, *Proc. Natl. Acad. Sci.* **112**, 14551 (2015).
- [65] M. B. Hastings, Lieb-Schultz-Mattis in higher dimensions, *Phys. Rev. B* **69**, 104431 (2004).
- [66] M. Oshikawa, Commensurability, excitation gap, and topology in quantum many-particle systems on a periodic lattice, *Phys. Rev. Lett.* **84**, 1535 (2000).
- [67] E. Lieb, T. Schultz, and D. Mattis, Two soluble models of an antiferromagnetic chain, *Ann. Phys.-new. York.* **16**, 407 (1961).